Angewandte Chemie International Edition
www.angewandte.org

How to cite: *Angew. Chem. Int. Ed.* **2025**, e202501151
doi.org/10.1002/anie.202501151

Electrochemiluminescence

Polychromatic Electrochemiluminescence Imaging of Single Heteroligand Metal–Organic Crystals

Yufei Wang, Tianrui Liu, Siqi Yu, Rengan Luo, Songsong Bao, Jie Wu, Huangxian Ju, Zhihui Dai,* and Jianping Lei**

Abstract: Conventional polychromatic electrochemiluminescence (ECL) imaging is realized with the several separated luminophores at the different potentials. In this study, an emerging polychromatic ECL imaging system was constructed based on single heteroligand metal–organic framework (MOF) crystals as nanoemitters through an intrareticular energy transfer process. The heteroligand MOF crystals, named h-NJU-241, were coassembled of *meso*-tetrakis(4-carboxyphenyl)porphyrin (TCPP) with 1,3,6,8-tetrakis(*p*-benzoic acid)pyrene (TBAPy) ligand using benzoic acid catalyst with coordination ability, leading to the conjugated spacing of 0.624 nm between two ligands. Remarkably, an energy transfer efficiency of 92.2% was achieved when the coordination weight ratio of TCPP acceptor and TBAPy donor was only 1.87‰. Different from monoligand MOFs, the heteroligand h-NJU-241 exhibits dual ECL emissions in both blue and red regions at one step applied potential, which is first example of polychromatic ECL imaging for single MOF crystals. Furthermore, by adjusting the reaction conditions, the morphology distribution of porphyrin within the crystal can be dynamically controlled, providing a tailored crystal platform for decoding fundamentals in polychromatic ECL imaging.

Introduction

Electrochemiluminescence (ECL) imaging is a powerful technique that harnesses electrode as light source under the applied potential or current.[1] Since this imaging technology boasts high sensitivity,[2] spatial resolution,[3] and chemical selectivity,[4] it has been extensively applied in biomedicine, environment, and material fields. Ongoing ECL imaging research efforts focus on the development of emerging ECL materials such as metal coordination complexes,[5] fluorescent organic molecules,[6] semiconductor nanoparticles,[7] organic-light-emitting diode materials,[8] and other nanocomposites.[9] In these materials, the restrictions imposed by Kasha's rule[10] frequently confine the emission of ECL emitters to a monochromatic wavelength. To realize polychromatic ECL imaging, integrating several monochromatic emitters into one hybrid material, such as ruthenium and iridium coordination complexes,[11,12] copolymer Janus particles,[13] and functional silicon composites from Paolucci's group,[14,15] is the primary strategy for emitting diverse colors.[16] Regardless of the method adopted, the predominant emitters with minimal interconnection are limited for the polychromatic ECL emission.[17] Moreover, the design and synthesis of composite materials present substantial challenges, often yielding structurally disordered, amorphous materials,[18] thus impeding targeted synthesis design. According to the atomic precise and skeleton rigid, the development of a single-particle crystalline material represents a promising prospect in ECL polychromatic imaging.[19]

Metal–organic frameworks (MOFs) as crystalline ECL emitters offer several advantages of tunable skeletons,[20,21] multifunctionality,[22] controllable optoelectronic properties,[23] and rapid charge transfer ability.[24,25] To meet the requirements of ECL imaging, it is essential that the MOF materials can produce sufficient ECL intensity. Typically, the strong ECL emission can be realized by incorporating donor–acceptor charge transfer motifs within the structure, and designing the linker as a coreactant.[26,27] Building upon this foundation, achieving multicolor emission in luminescent materials necessitates the presence of multiple excited states.[28–30] A common strategy involves the construction of mixed ligand MOFs with diverse absorption-emission domains, wherein ligands with distinct transition energy levels are employed.[31] The assembly of guest molecules as excitation levels in the porous MOFs also leads to guest-dependent charge-transfer based emissions.[32,33] Additionally, modifying predetermined MOF defect structures by introducing other ligands with differing energy characteristics is a viable strategy.[34] Alternatively, by coordinating size-resembled ligands with nodes, the

---

[*] Y. Wang, T. Liu, Dr. S. Yu, Dr. R. Luo, Prof. Dr. S. Bao, Prof. Dr. J. Wu, Prof. Dr. H. Ju, Prof. Dr. Z. Dai, Prof. Dr. J. Lei
State Key Laboratory of Analytical Chemistry for Life Science, School of Chemistry and Chemical Engineering, Nanjing University, Nanjing 210023, China
E-mail: wujie@nju.edu.cn
daizhihuii@njnu.edu.cn
jpl@nju.edu.cn

Prof. Dr. Z. Dai
Collaborative Innovation Center of Biomedical Functional Materials, Key Laboratory of Biofunctional Materials of Jiangsu Province, School of Chemistry and Materials Science, Nanjing Normal University, Nanjing 210023, China

Additional supporting information can be found online in the Supporting Information section resulting heteroligand MOFs with precise modification and functionalization present a new avenue to modulate multiple excited states.[35] Indeed, strategies for constructing heteroligand MOFs are being explored in optical and photocatalytic research domains,[36,37] offering promising prospects for their applications in ECL imaging.

In terms of principles, the ECL emission of MOF crystals bears certain similarities to crystallization induced ECL,[38] inherent to the emission itself. To devise heteroligand MOFs tailored for multicolor ECL imaging, several hurdles must be surmounted beyond ensuring adequate ECL emission intensity as follows: first, the ligands composing the heteroligand MOF must exhibit compatible energy levels and possess the capacity for efficient energy transfer (ET) between them.[39] Second, the spatial arrangement of ligands and the interlayer distance between conjugated ligands warrant careful consideration. A minimal π spacing between conjugated ligands may result in molecular spectral redshift and an increased contribution of molecular relaxation vibrations, leading to heightened energy dissipation due to π–π interactions. Finally, meticulous selection of nodal metal ions is imperative. Analogous to fluorescence, the ligand to metal charge transfer effect[40] can profoundly attenuate the ECL emission capability of ligands within MOFs. Furthermore, the presence of high-valent metal clusters such as Zr(IV), exemplified by $[Zr_6O_8]$ cluster, inherently possesses radical quenching ability to reduce the ECL of MOFs.[41] These challenges arouse us to design efficient heteroligand MOF systems for polychromatic ECL imaging.

In this work, to realize polychromatic ECL imaging, we employed the fluorescent ligand 1,3,6,8-tetrakis(*p*-benzoic acid)pyrene (TBAPy) with 40% fluorescence quantum yield as a qualified electron donor, along with the corresponding energy-accepting ligand *meso*-tetrakis(4-carboxyphenyl)porphyrin TCPP, to construct the heteroligand MOF (h-NJU-241). Different from the singular imaging of TBAPy and TCPP monoligand MOFs, the heteroligand h-NJU-241 exhibits excellent polychromatic ECL imaging in both blue and red regions at one-step potential. Significantly, an intrareticular energy transfer efficiency of 92.2% was achieved due to the large conjugated spacing (0.624 nm), even when the coordination weight ratio of TCPP to TBAPy was down to 1.87‰. Furthermore, the morphological distribution of porphyrins can be dynamically controlled at the specific sites, providing a paradigm of crystalline nanoemitters in robust polychromatic ECL imaging.

Results and Discussion

The single crystals with the chemical formula $[Mg(TBAPy)(DMF)_2]\cdot 3DMF$ (CCDC deposition number: 2322488)[42] and $[Mg(TCPP)(DMF)_2]\cdot 5DMF$ (CCDC deposition number: 2322225)[43] were synthesized by using TBAPy and TCPP monoligands through a closed solvothermal approach, which are designated as NJU-241 and NJU-242, respectively. As both TCPP and TBAPy ligands have a similar size, a heteroligand MOF named h-NJU-241 was obtained by coassembly of TCPP within the NJU-241 crystal network (Figure 1a). The monoclinic crystal structure of NJU-241, characterized by a typical pts-type topology and belonging to the $C2/c$ space group (Figure S1), is notable within the field of magnesium MOF (MgMOF) due to its exceptional pore architecture. Similarly, the porphyrin-based MOF NJU-242 crystallizes in the $P2_1/n$ space group and exhibits a comparable pts topological structure (Figure S2). Considering the complexation of Mg(II) with COO^- within an octahedral field, the COO^- moiety adopts a nonsaturation coordination mode characterized by a spatial arrangement between the O···O with a distance of 0.245 nm (Figure 1a). The NJU-241 single crystal is a rod-shaped, pale yellow transparent crystal (Figure 1b), exhibiting blue fluorescence from pyrene under UV light. The h-NJU-241 shares the same rod-like crystal morphology as NJU-241 (Figure 1c) while displaying the characteristic crimson of porphyrin. Under UV light irradiation, it exhibits blue and red fluorescence, whereas red light becomes more obvious with increasing porphyrin content. Conversely, NJU-242 is a red-black rod-shaped crystal, displaying red fluorescence from porphyrin under UV light (Figures 1d and S3). This unique configuration not only contributes to the overall structural stability but also facilitates the insertion of redox molecules, underscoring the potential of NJU-241 or NJU-242 in intriguing reactivity and electrochemical properties.

The powder X-ray diffraction (PXRD) patterns of two monoligand MOFs closely aligned with the simulated crystal formula patterns (Figure 1e,g). Notably, the PXRD spectra of these heteroligand h-NJU-241 consistently exhibited diffraction patterns identical to those of the monoligand MOF NJU-241 (Figure 1f). The mass ratios representing these diverse coordination levels of porphyrin to pyrene within the h-NJU-241 MOFs were determined using high-performance liquid chromatography–mass spectrometry (Figure S4). Compared to pyrene, the mass fraction of porphyrin was remarkably low, ranging from 0.39‰ to 1.87‰, corresponding to porphyrin-to-pyrene feed ratios of merely 1.0%–10%. Upon exceeding a porphyrin feed ratio of 10%, NJU-241 exhibited the increased disorder attributed to distinct ligand configurations, resulting in a loss of crystallinity evidenced by the absence of characteristic diffraction peaks in the PXRD spectra (Figure S5). Due to the exceedingly low coordination ratio of porphyrin, this series of h-NJU-241 MOFs exhibits nearly identical chemical structural characteristics to the monoligand NJU-241.

The selected area electron diffraction patterns (SAED) obtained from high-resolution transmission electron microscopy (HR-TEM) of NJU-241 exhibits a typical single-crystal diffraction pattern, with lattice spacing of 1.76 nm corresponding to its (110) crystal plane (Figure S6). h-NJU-241 shows nearly identical diffraction lattice to NJU-241, attributed to the structural similarity resulting from porphyrin substitution coordination (Figure S7). NJU-242 also displays the corresponding single-crystal diffraction pattern, with a lattice spacing of 1.80 nm corresponding to its (110) crystal plane (Figure S8). Further, these MOFs are evident in Fourier-transform infrared spectroscopy (FT-IR) and carbon-13 solid-state nuclear magnetic resonance spectra (Figures S9–S12). The h-NJU-241 unequivocally coordinated by porphyrin ligands verifies the low coordination rate

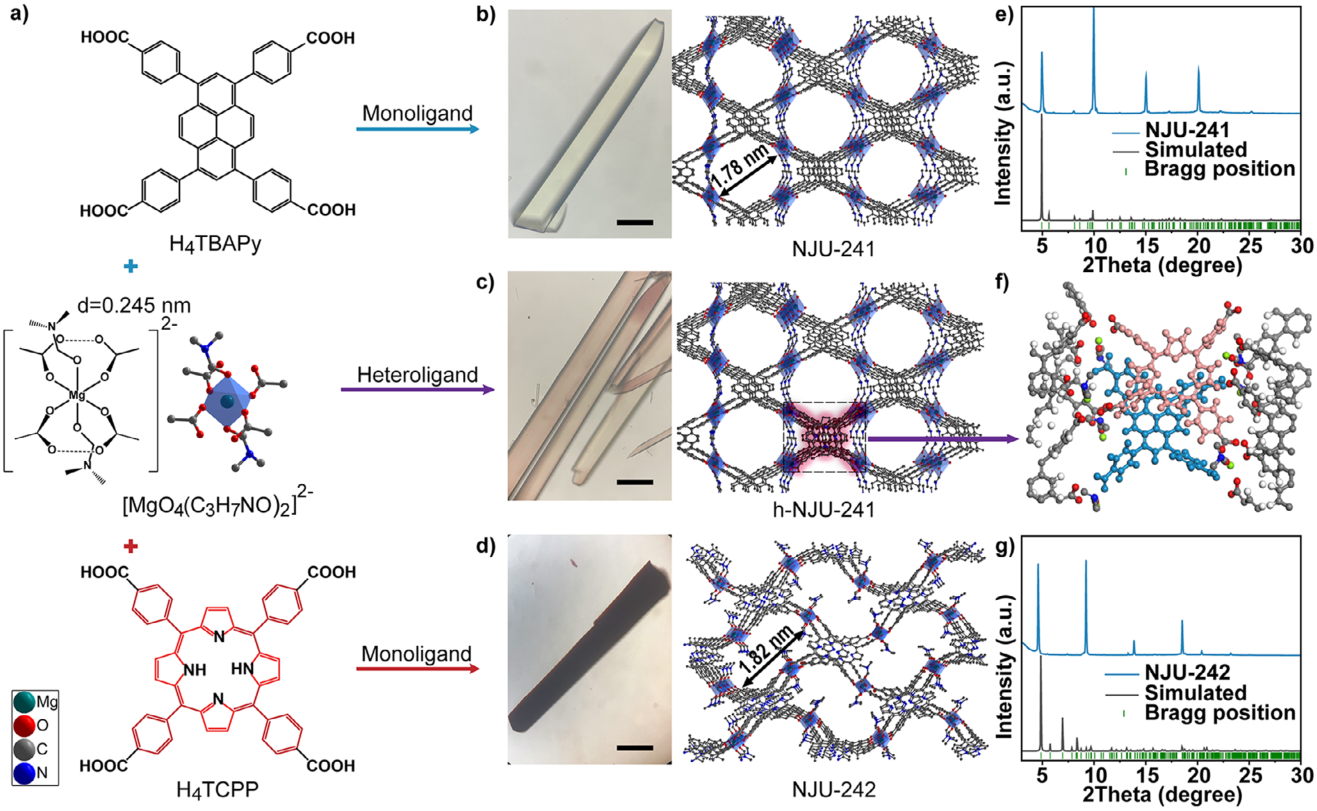

Figure 1. Schematic diagrams of a) the preparation of a series of Mg-MOFs by using individual pyrene and porphyrin as monoligands or mixing both as heteroligand. The single crystal images and top view structures of b) NJU-241, c) h-NJU-241, and d) NJU-242. Scale bar: 200 μm. PXRD spectra of e) NJU-241 and g) NJU-242. f) Porphyrin/pyrene heteroligand within h-NJU-241 unit cell.

of porphyrin within these MOFs, allowing sufficient efficiency in ET in both photochemical and electrochemical properties.

The ECL properties of NJU-241, h-NJU-241, and NJU-242 are illustrated in Figure 2a. In the presence of 20 mM tripropylamine (TPrA) coreactant, the NJU-241 modified electrode displays a highly intense ECL emission peak under 400 V of photomultiplier tube voltage (PMT) at +0.87 V, which is attributed to the direct oxidation of the pyrene core with irreversible electrochemical characterization (Figures S13–S15). Similarly, h-NJU-241 MOFs initially exhibit the same intrinsic ECL emission peak at +0.87 V. Moreover, these intrinsic ECL emission peaks gradually decreased with the increase of the coordination ratios of porphyrin within the h-NJU-241, along with a new ECL emission peak at +1.0 V. Specifically, when the coordination ratio of porphyrin reaches 1.87‰, the intensity of this intrinsic ECL peak at +0.87 V is only approximately 1/6 of that observed for NJU-241 as the current density remains relatively constant (Figure S16). Different from the low ECL peak of porphyrin in NJU-242, the enhancement ECL of porphyrin in h-NJU-241 is probably attributed to the emission from the porphyrin excited by energy transfer.

To elucidate the ET process in ECL, the ECL spectra of NJU-241 and h-NJU-241 were collected, which exhibited a gradual decrease in intrinsic blue emission from pyrene molecules (Figures S17 and S18) and a concurrent increase in red emission from porphyrin molecules as the coordination ratio of porphyrin increased (Figure 2b). Below a mass ratio of 1.34‰ por, the ECL emission of the MOF is predominantly blue emission from pyrene. Upon surpassing this ratio, the intrinsic emission from pyrene gradually diminishes and eventually disappears at mass ratio of 1.87‰ por while the predominant component of ECL shifts to red emission from porphyrin, suggesting a high intrareticular ET efficiency between pyrene and porphyrin in h-NJU-241 (Figure S19). It is noteworthy that there are no direct bonds between the coordinating Mg(II) ions in the lattice elements of the framework, and such structural flexibility provides favorable conditions for the loose growth of ligands within the MOF structure, leading to the interplanar distance of $d = 0.624$ nm between pyrene molecules in NJU-241 (Figure 2c). Thus, the aggregation-caused quenching can be effectively suppressed with enhanced ECL emission efficiency expressed as the ratio of emitted photons to electrons consumed during the electrochemical process (Figure S20). To confirm this, other Mg-based pyrene MOFs, such as TDL-Mg,[44] MIT-26,[45] and SION-7,[46] were synthesized with the π spacing between pyrene molecules ranging from 0.322 to 0.361 nm due to the binding interaction among Mg ions (Figures S21–S24), which exhibited the significantly reduced ECL intensity (Figure 2d). Under the same molar amount of pyrene, SION-7 with a pyrene π spacing of 0.322 nm exhibited only 12% of an integrated ECL intensity of NJU-241. In NJU-241, such structural

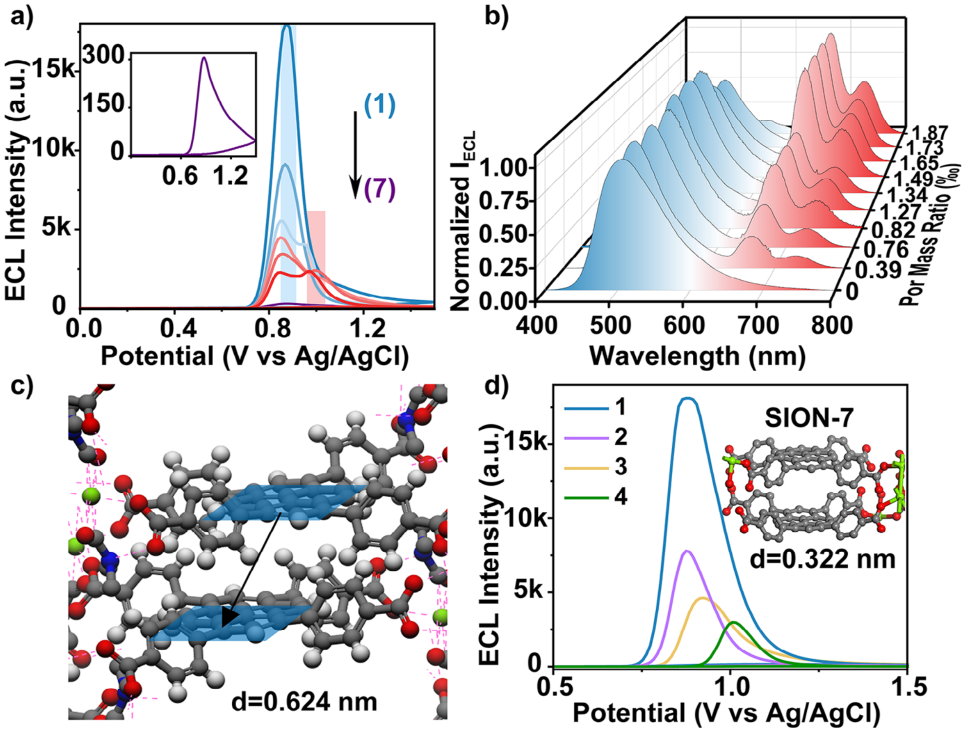

Figure 2. a) ECL curves of (1) NJU-241, h-NJU-241 with (2) 0.39‰, (3) 0.82‰, (4) 1.34‰, (5) 1.65‰, (6) 1.87‰ por, and (7) NJU-242 modified GCEs in 0.1 M Tris·HCl buffer containing 20 mM TPrA. b) Dependence of ECL spectra on por mass rations of h-NJU-241. c) Schematic illustration of pyrene–pyrene distance in NJU-241. d) ECL performance of (1) NJU-241, (2) TDL-Mg, (3) MIT-26, and (4) SION-7 modified GCEs in 0.1 M Tris·HCl buffer containing 20 mM TPrA. Inset: pyrene–pyrene distance in SION-7. PMT = 400 V.

characteristic with broad π spacing between pyrene molecules provided a promising way to enhance ECL efficiency.

To further verify the ET mechanism of MOFs, we depict the fluorescence spectroscopic characterization of NJU-241 and h-NJU-241. The solid-state fluorescence spectroscopy of both MOFs, excited by 365 nm light, exhibited similar features to the ECL spectra described before (Figure 3a). Compared to the ECL spectra, both the intrinsic emissions of pyrene and porphyrin in the solid-state fluorescence spectra of MOFs exhibit a certain extent of blueshift and narrower peaks, attributed to the absence of solvatochromic effect.[47,48] Moreover, with the increase of porphyrin coordination ratio, the emission change from 460 to 650 nm in the solid-state fluorescence spectra becomes more pronounced, which is attributed to the shift of intrinsic emission from pyrene to porphyrin. It is important to note that, whether it is the H_4TCPP ligand or the porphyrin NJU-242, the fluorescence emissions originating from porphyrin are very weak due to strong interlayer π–π interactions, making them incomparable to the intense fluorescence from the pyrene moiety. Subsequently, when the coordination ratio of porphyrin exceeds 1.27‰, it is observed that the intrinsic emission peak of pyrene at 460 nm becomes asymmetric, and the fluorescence intensity at 650 nm significantly increases, confirming the intrareticular energy transfer from pyrene to porphyrin in the MOF skeleton.

In the energy transfer system, the excited-state lifetime serves as an important physical parameter for measuring the rate and efficiency of energy transfer. The fluorescence lifetime decay spectra of NJU-241 and h-NJU-241, excited at 365 nm and emitting at 455 nm, are depicted in Figure 3b. The emission at 455 nm corresponds to the π^*–π emission of pyrene. It can be observed that as the coordination ratio of porphyrin gradually increases, the fluorescence lifetime of pyrene significantly decreases. For NJU-241, the lifetime of pyrene at 455 nm is 8.48 ns. Meanwhile, in the presence of a low amount of porphyrin (0.39‰) as acceptor, the lifetime of equivalent h-NJU-241 rapidly decreases to 2.42 ns, demonstrating a significant manifestation of energy transfer. When the porphyrin mass ratio reaches 1.87‰, the fluorescence lifetime at 455 nm is only 0.69 ns, ensuring high fluorescence quantum yield. In contrast, at the emission wavelength of 655 nm for porphyrin (Figure S25), there was almost no change in the fluorescence lifetime as the porphyrin mass ratio increased.

Using a photon integrating sphere, the absolute fluorescence quantum yield of the material can be measured in the presence of pump light with a known number of photons. As depicted in Figure 3c with logarithmic y axis, NJU-241 exhibits an absolute fluorescence quantum yield as high as 40%. However, the absolute fluorescence quantum yield of h-NJU-241 rapidly decreases as the amount of porphyrin increases, even with nearly constant photon absorption. The decrease can be attributed to both energy losses during ET and the inefficient fluorescence of porphyrin, where only a portion of the absorbed energy contributes to fluorescence emission.[49,50] This process is evident in Figure S26, where both the H_4TCPP ligand and pure porphyrin NJU-242 exhibit negligible absolute fluorescence quantum yields.

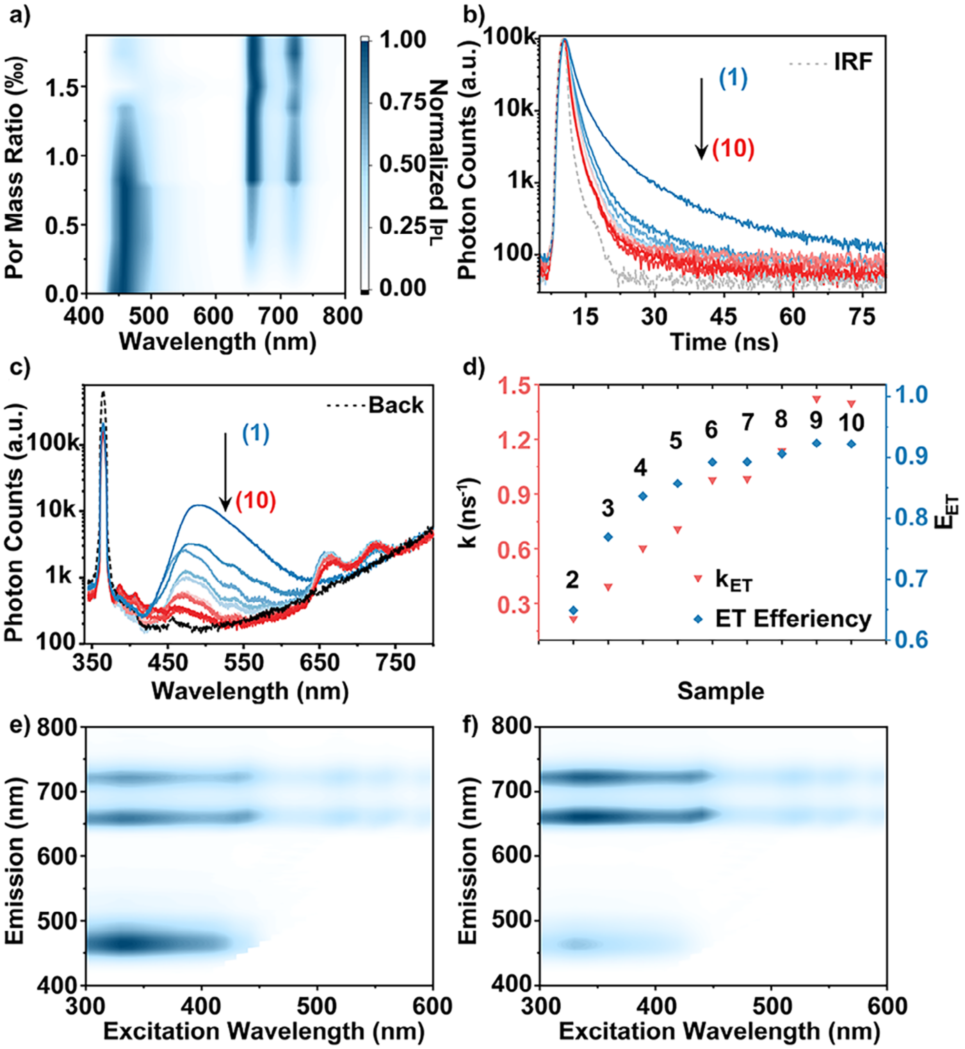

Figure 3. a) Solid state photoluminescence spectra of h-NJU-241 with por mass ratios from 0.39 to 1.87‰. b) Fluorescence lifetimes at 465 nm and c) solid state fluorescence spectra with a pump light of 365 nm for (1) NJU-241, (2–10) h-NJU-241 with 0.39‰, 0.76‰, 0.82‰, 1.27‰, 1.34‰, 1.49‰, 1.65‰, 1.73‰, and 1.87‰ por, individually, and d) relative dynamic reaction rate constant and E_{ET} of h-NJU-241. e,f) 3D fluorescence spectra of h-NJU-241 (0.76‰ por) and h-NJU-241 (1.34‰ por).

Combining the fluorescence lifetime and fluorescence quantum yield mentioned above, the energy transfer rate constant (k_{ET}) and energy transfer efficiency (E_{ET}) of h-NJU-241 as a function of porphyrin concentration can be calculated. The detailed results are described in Figure 3d and Table 1. Both k_{ET} and E_{ET} are positively correlated with the porphyrin coordination ratio. When the porphyrin coordination ratio reaches 1.87‰, the kinetic rate constant and the efficiency reach 0.924 ns^{-1} and 92.2%, respectively. The ET efficiency of h-NJU-241 is among the highest in reticular luminophores,[51–54] which is beneficial for the spatial arrangement of pyrene and porphyrin in h-NJU-241 and the broad π-spacing.

To further assess the reticular ET behavior, the 3D fluorescence spectra of h-NJU-241 with por mass ratios from 0‰ to 1.87‰ and NJU-242 were measured, as shown in Figure S27. NJU-241 exhibits a robust intrinsic emission peak of pyrene at 450–550 nm, whereas NJU-242 shows almost no emission band at 655 nm, with only emission at 720 nm. As the porphyrin ratio increases, the emission band at 655 nm becomes increasingly prominent, whereas the intrinsic emission of pyrene gradually weakens. At 0.39‰

Table 1: Energy transfer dynamic constant of NJU-241 and h-NJU-241.

Por (‰)	τ_μ (ns)	E_{FRET} (%)	Φ %	k_{ET} (ns^{-1})	E_{ET} (%)
0	8.48	–	40.00	–	–
0.39	2.42	71.4	14.05	0.218	64.9
0.76	2.09	75.4	9.22	0.332	76.9
0.82	2.06	75.7	6.54	0.468	83.6
1.27	1.98	78.9	5.71	0.536	85.7
1.34	1.73	79.6	4.30	0.813	89.3
1.49	1.63	80.8	4.28	0.711	89.3
1.65	1.55	81.7	3.77	0.715	90.6
1.73	1.45	82.9	3.06	0.999	92.3
1.87	0.69	91.9	3.31	0.924	92.2

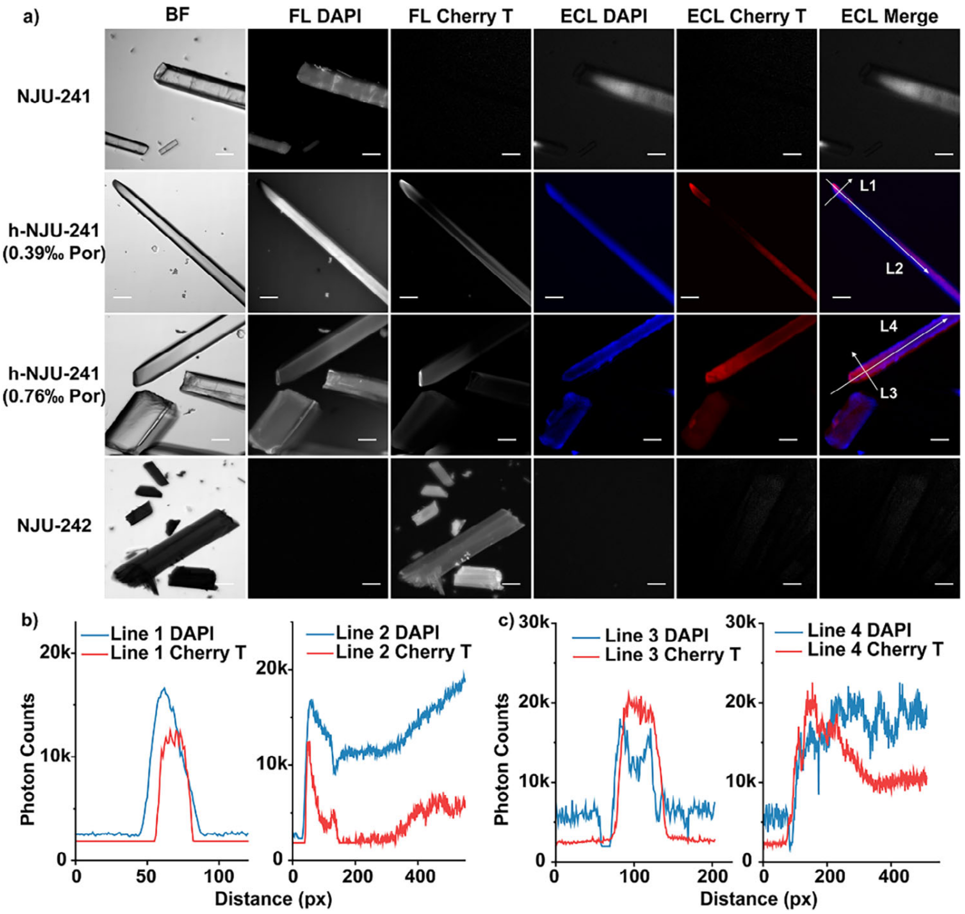

Figure 4. a) Images of bright field, fluorescence DAPI and Cherry-T channels, and ECL DAPI and Cherry-T channels captured by EMCCD for NJU-241, h-NJU-241 (0.39‰ por), h-NJU-241 (0.76‰ por), and NJU-242. b,c) Intensity plots for ECL merge channels of h-NJU-241 (0.39‰ por) and h-NJU-241 (0.76‰ por) alongside radial (L1, L3) and axial direction lines (L2, L4). Electrolyte: 0.1 M pH 7.4 Tris·HCl buffer containing 20 mM TPrA and 0.1 M KNO_3. Scale bar: 100 µm.

porphyrin concentration, the relative emission intensity ratio of pyrene to porphyrin is 7:1 upon excitation at 340 nm. As a comparison, at 1.87‰, it becomes 1:12, further indicating the energy transfer from pyrene to porphyrin (Figures S28 and S29). Meanwhile, Figure 3e,f demonstrate that as the excitation wavelength increases from 300 to 460 nm, the emission intensity of pyrene gradually increases, reaching its maximum at 340 nm, and then gradually decreases. Correspondingly, the emission intensity of porphyrin also exhibits an increase followed by a decrease in response to the change in pyrene. In the excitation wavelength range of 460–600 nm, where pyrene is no longer excited, porphyrin exhibits extremely weak emission, approximately 1/6 of that at 340 nm excitation in Figure 3e and only 1/8 in Figure 3f. Overall, the intensive emission of porphyrin in h-NJU-241 is attributed to the high efficiency of intrareticular energy transfer between pyrene and porphyrin rather than the directly exciting porphyrin molecules.

Based on the above multiple emission features and stable ECL characteristics of heteroligand MOFs (Figure S30), their single crystals can be utilized for polychromatic ECL imaging. Due to these stringent requirements including surface flatness,[55] degree of fit with the electrode surface, and the size of single crystal,[56] researchers have not yet applied MOF single crystals as emitters for ECL imaging. For NJU-241 and h-NJU-241 MOFs, their single crystals are regularly shaped rod-like crystals with extremely high crystallinity, appropriate thickness, low electrochemical impedance (Figure S31), and high transparency, making them suitable for ECL imaging of single crystals. By integrating a super-resolution radial fluctuation algorithm as a correction method,[57–61] the specific ECL imaging results with the enhanced grayscale contrast and resolution are presented in Figure 4. Different from conventional monochromatic ECL imaging, NJU-241 and h-NJU-241 single crystals provide a sufficient number of imaging photons to enable multispectral imaging. It can be observed that NJU-241, h-NJU-241 (0.39‰ por), and h-NJU-241 (0.76‰ por) exhibit consistent fluorescence-ECL in both the blue channel DAPI and the red channel Cherry-T (Figure 4a), demonstrating excellent ECL single-crystal imaging capabilities confined to the surface-adjacent region. On the other hand, the porphyrin-based NJU-242, due to its limited ECL effect, is unavailable as a single-crystal emitter for imaging. Therefore, this is a useful means of using heteroligand MOFs to obtain porphyrin-colored light in ECL imaging, replacing poorly performing porphyrin MOFs.

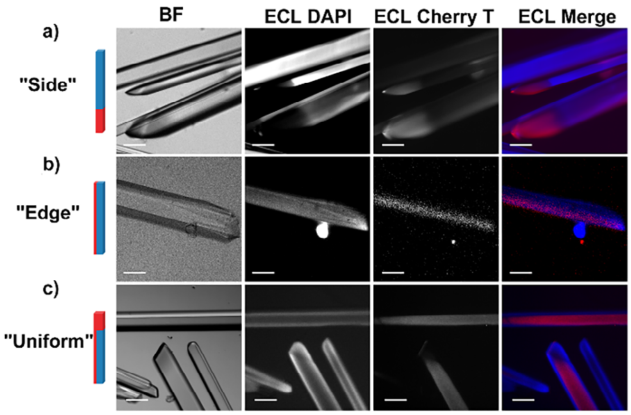

Figure 5. ECL imaging performance for a) side, b) edge, and c) uniform crystallization pattern modes by coassembled TCPP into NJU-241 in different reaction conditions: 403 K for 48 h following with 393 K for 48 h, 403 K for 72 h, and 393 K for 72 h, respectively. Electrolyte: 0.1 M Tris·HCl buffer (pH 7.4) containing 20 mM TPrA and 0.1 M KNO_3. Scale bar: 100 μm.

To investigate the spatial relationship of the ECL in MOF crystals, lines L1–L4 are drawn to illustrate the distribution of photon counts as a function of distance from the starting point (Figure 4a). The intensity analysis of the ECL merge image demonstrated that the positions of the blue and red light, emitted by the MOF single crystals, are not entirely consistent (Figure 4b,c), influenced by multiple factors. Firstly, the uneven distribution of porphyrin in the heteroligand MOFs, particularly evident in h-MOF-241 (0.39‰ por). The fluorescence image also reveals a noticeable absence of porphyrin in the crystal's 200–350 px region, and its ECL distribution corresponds to the fluorescence distribution structure. Secondly, to some extent, the boundary distribution of blue light is finer compared to red light as shorter wavelength light has a smaller Gaussian diffraction radius.[2] Overall, based on the excellent wavelength resolution and spatial resolution, h-NJU-241's polychromatic ECL imaging is suitable for simultaneous detection of multiple luminescent signals, offering a more comprehensive understanding of sample composition and ECL properties.[62]

To adjust the distribution of porphyrin within single crystals, we optimized the synthesis method of the heteroligand MOFs. Under conditions of 403 K for 48 h following with 393 K for 48 h, crystals with "side" morphology were observed (Figure 5a). The distribution of porphyrin could be controlled by reaction kinetics, that is, at an ambient temperature of 403 K, the assembly rate of the porphyrin ligand is highly dynamical and predominant during the initial formation of MOF. Upon the reaction temperature lowered to 393 K, the assembly of the pyrene ligand continues to thermodynamically grow along the previously concentrated direction of porphyrin,[63,64] resulting in crystals with a "side" morphology (Figure 5a). At the reaction temperature down to 363 K with the decreased concentration of the competing agent, targeting nanocrystals with a size distribution of ~100 nm can be obtained (Figure S32). Conversely, when the growth is maintained at 403 K, the pyrene ligand could exchange with porphyrin at a slower rate and correct the overly dense structure of porphyrin with a thermodynamic equilibrium, leading to the crystals with an "edge" morphology (Figure 5b). Additionally, maintaining the temperature at 393 K throughout the synthesis leads to the simultaneous assembly and precipitation of both pyrene and porphyrin ligands at a slower rate, resulting in a more homogeneous "uniform" structure (Figure 5c). In summary, for heteroligand MOFs, the morphology distribution can be dynamically controlled according to specific application requirements, making them ideal crystals for polychromatic ECL imaging.

Conclusion

We have successfully established a polychromatic ECL system based on heteroligand MOFs via the intrareticular energy-transfer pathway. Benefiting from the favorable spatial arrangement between the donor pyrene and acceptor porphyrin moieties, the heteroligand MOF exhibits an energy transfer efficiency of 92.2%. Significantly, the intrareticular energy transfer kinetic constant enhanced 4.5-fold with the increase of porphyrin coordination ratios to 1.87‰. At applying one-step potential, heteroligand MOFs exhibit the distinct dual-wavelength emission with intensive intensity, comparable to the equivalent $Ru(bpy)_3^{2+}$ system. Furthermore, taking advantages of high crystallinity, appropriate thickness, good conductivity, and high transparency, single heteroligand MOF crystals achieved polychromatic ECL imaging with excellent spatial resolution for the first time, making them highly desirable for a variety of practical applications such as multiplexed detection and crystal heterogeneity research. Moreover, by fine-tuning the distribution of porphyrin within the crystal lattice, heteroligand MOFs offer an engineered crystal matrix to facilitate a deeper insight into the ECL imaging characteristics and relating reaction processes.

Acknowledgements

The authors gratefully acknowledge the Natural Science Foundation of Jiangsu Province (BZ2021010) and National Natural Science Foundation of China (22274071, 22234005).

Conflict of Interests

The authors declare no conflict of interest.

Data Availability Statement

The data that support the findings of this study are available in the Supporting Information of this article.

Keywords: Electrochemiluminescence • Energy transfer • Metal–organic frameworks • Polychromatic imaging • Single crystals

---

[1] J. Dong, Y. Lu, Y. Xu, F. Chen, J. Yang, Y. Chen, J. Feng, *Nature* **2021**, *596*, 244–249.

[2] Y. Wang, J. Ding, P. Zhou, J. Liu, Z. Qiao, K. Yu, J. Jiang, B. Su, *Angew. Chem. Int. Ed.* **2023**, *62*, e202216525.

[3] H. Ding, W. Guo, B. Su, *Angew. Chem. Int. Ed.* **2020**, *59*, 449–456.

[4] X. Zhao, Y. Li, Y. Cui, M. Saqib, X. Zhang, R. Hao, Z. Zheng, *J. Am. Chem. Soc.* **2023**, *145*, 20897–20906.

[5] Y. Lu, X. Huang, S. Wang, B. Li, B. Liu, *ACS Nano* **2023**, *17*, 3809–3817.

[6] Y. Zhang, Y. Zhao, Z. Han, R. Zhang, P. Du, Y. Wu, X. Lu, *Angew. Chem. Int. Ed.* **2020**, *59*, 23261–23267.

[7] L. Li, Z. Zhang, Y. Chen, Q. Xu, J. Zhang, Z. Chen, Y. Chen, J. Zhu, *Adv. Funct. Mater.* **2019**, *29*, 1902533.

[8] J. W. Oh, J. Y. Jeong, T. Y. Eom, S. D. Baek, J. M. Myoung, *Chem. Eng. J.* **2021**, *416*, 129202.

[9] T. Ikeda, K. Tahara, R. Ishimatsu, T. Ono, L. Cui, M. Maeda, Y. Ozawa, M. Abe, *Angew. Chem. Int. Ed.* **2023**, *62*, e202301109.

[10] A. P. Demchenko, V. I. Tomin, P. T. Chou, *Chem. Rev.* **2017**, *117*, 13353–13381.

[11] Y. Z. Wang, C. H. Xu, W. Zhao, Q. Y. Guan, H. Y. Chen, J. J. Xu, *Anal. Chem.* **2017**, *89*, 8050–8056.

[12] S. Voci, R. Duwald, S. Grass, D. J. Hayne, L. Bouffier, P. S. Francis, J. Lacour, N. Sojic, *Chem. Sci.* **2020**, *11*, 4508–4515.

[13] T. Han, C. Ma, L. Wang, Y. Cao, H. Y. Chen, J. J. Zhu, *Adv. Funct. Mater.* **2022**, *32*, 2200863.

[14] G. Valenti, E. Rampazzo, S. Bonacchi, T. Khajvand, R. Juris, M. Montalti, M. Marcaccio, F. Paolucci, L. Prodi, *Chem. Commun.* **2012**, *48*, 4187–4189.

[15] G. Morselli, F. Romano, G. Valenti, F. Paolucci, P. Ceroni, *J. Phys. Chem. C* **2021**, *125*, 5708–5714.

[16] L. Wang, Z. G. Wang, D. Ning, Y. Hu, S. L. Liu, D. W. Pang, *Nano Today* **2023**, *50*, 101855.

[17] Z. Cao, Y. Shu, H. Qin, B. Su, X. Peng, *ACS Cent. Sci.* **2020**, *6*, 1129–1137.

[18] F. Li, Y. Xi, J. Jiang, H. Peng, B. Li, J. He, J. Shu, H. Cui, *Anal. Chem.* **2022**, *94*, 9306–9315.

[19] W. Guo, H. Ding, P. Zhou, Y. Wang, B. Su, *Angew. Chem. Int. Ed.* **2020**, *59*, 6745–6749.

[20] T. Liu, Q. Tao, Y. Wang, R. Luo, J. Ma, J. Lei, *J. Am. Chem. Soc.* **2024**, *146*, 18958–18966.

[21] W. Chen, Z. Wang, Q. Wang, K. El-Yanboui, K. Tan, H. M. Barkholtz, D. J. Liu, P. Cai, L. Feng, Y. Li, J. S. Qin, S. Yuan, D. Sun, H. C. Zhou, *J. Am. Chem. Soc.* **2023**, *145*, 4736–4745.

[22] B. Li, X. Huang, Y. Lu, Z. Fan, B. Li, D. Jiang, N. Sojic, B. Liu, *Adv. Sci.* **2022**, *9*, 2240715.

[23] C. Kaiyasuan, V. Somjit, B. Boekfa, D. Packwood, P. Chasing, T. Sudyoadsuk, K. Kongpatpanich, V. Promarak, *Angew. Chem. Int. Ed.* **2022**, *61*, e202117608.

[24] R. Luo, X. Luo, H. Xu, S. Wan, H. Lv, B. Zou, Y. Wang, T. Liu, C. Wu, Q. Chen, S. Yu, P. Dong, Y. Tian, K. Xi, S. Yuan, X. Wu, H. Ju, J. Lei, *J. Am. Chem. Soc.* **2024**, *146*, 16681–16688.

[25] J. Y. Zeng, X. S. Wang, B. R. Xie, Q. R. Li, X. Z. Zhang, *J. Am. Chem. Soc.* **2022**, *144*, 1218–1231.

[26] K. Song, W. Zhao, Y. Zhou, D. Liu, P. K. Chu, *Coordin. Chem. Rev.* **2024**, *520*, 216161.

[27] R. Luo, D. Zhu, H. Ju, J. Lei, *Acc. Chem. Res.* **2023**, *56*, 1920–1930.

[28] X. Meng, L. Zheng, R. Luo, W. Kong, Z. Xu, P. Dong, J. Ma, J. Lei, *Angew. Chem. Int. Ed.* **2024**, *63*, e202402373.

[29] S. Yu, Y. Du, X. Niu, G. Li, D. Zhu, Q. Yu, G. Zou, H. Ju, *Nat. Commun.* **2022**, *13*, 137302.

[30] P. Fang, L. Qu, Z. Ma, C. Han, Z. Li, L. Wang, K. Zhou, J. Li, X. Liu, *Angew. Chem. Int. Ed.* **2024**, *63*, e202414026.

[31] C. Fiankor, J. Nyakuchena, R. S. H. Khoo, X. Zhang, Y. Hu, S. Yang, J. Huang, J. Zhang, *J. Am. Chem. Soc.* **2021**, *143*, 20411–20418.

[32] X. T. Liu, K. Wang, Z. Chang, Y. H. Zhang, J. Xu, Y. S. Zhao, X. H. Bu, *Angew. Chem. Int. Ed.* **2019**, *58*, 13890–13896.

[33] D. S. Zhang, Q. Gao, Z. Chang, X. T. Liu, B. Zhao, Z. H. Xuan, T. L. Hu, Y. H. Zhang, J. Zhu, X. H. Bu, *Adv. Mater.* **2018**, *30*. 1804715.

[34] P. Cai, M. Xu, S. S. Meng, Z. Lin, T. Yan, H. F. Drake, P. Zhang, J. Pang, Z. Y. Gu, H. C. Zhou, *Angew. Chem. Int. Ed.* **2021**, *60*, 27258–27263.

[35] J. Perego, C. X. Bezuidenhout, I. Villa, F. Cova, R. Crapanzano, I. Frank, F. Pagano, N. Kratochwill, E. Auffray, S. Bracco, A. Vedda, C. Dujardin, P. E. Sozzani, F. Meinardi, A. Comotti, A. Monguzzi, *Nat. Commun.* **2022**, *13*, 133504.

[36] B. Lerma-Berlanga, C. R. Ganivet, N. Almora-Barrios, S. Tatay, Y. Peng, J. Albero, O. Fabelo, J. González-Platas, H. García, N. M. Padial, C. Martí-Gastaldo, *J. Am. Chem. Soc.* **2021**, *143*, 1798–1806.

[37] S. Knežević, D. Han, B. Liu, D. Jiang, N. Sojic, *Angew. Chem. Int. Ed.* **2024**, *63*, e202407588.

[38] J. M. Wong, R. Zhang, P. Xie, L. Yang, M. Zhang, R. Zhou, R. Wang, Y. Shen, B. Yang, H. B. Wang, Z. Ding, *Angew. Chem. Int. Ed.* **2020**, *59*, 17461–17466.

[39] C. R. Martin, K. C. Park, G. A. Leith, J. Yu, A. Mathur, G. R. Wilson, G. B. Gange, E. L. Barth, R. T. Ly, O. M. Manley, K. L. Forrester, S. G. Karakalos, M. D. Smith, T. M. Makris, A. K. Vannucci, D. V. Peryshkov, N. B. Shustova, *J. Am. Chem. Soc.* **2022**, *144*, 4457–4468.

[40] Y. Guo, X. Feng, T. Han, S. Wang, Z. Lin, Y. Dong, B. Wang, *J. Am. Chem. Soc.* **2014**, *136*, 15485–15488.

[41] S. Cheng, J. Ouyang, M. Li, Y. Diao, J. Yao, F. Li, Y. F. Lee, H. H. Y. Sung, I. Williams, Z. Xu, Y. Quan, *Angew. Chem. Int. Ed.* **2023**, *62*, e202300993.

[42] Deposition Number 2322488 (for NJU-241) contains the supplementary crystallographic data for this paper. These data are provided free of charge by the joint Cambridge Crystallographic Data Centre and Fachinformationszentrum Karlsruhe (http://www.ccdc.cam.ac.uk/structures) Access Structures service.

[43] Deposition Number 2322225 (for NJU-242) contains the supplementary crystallographic data for this paper. These data are provided free of charge by the joint Cambridge Crystallographic Data Centre and Fachinformationszentrum Karlsruhe (http://www.ccdc.cam.ac.uk/structures) Access Structures service.

[44] Z. Hu, C. Qiao, Z. Xia, F. Li, J. Han, Q. Wei, Q. Yang, G. Xie, S. Chen, S. Gao, *ACS Appl. Mater. Inter.* **2020**, *12*, 14914–14923.

[45] S. S. Park, C. H. Hendon, A. J. Fielding, A. Walsh, M. O'Keeffe, M. Dincă, *J. Am. Chem. Soc.* **2017**, *139*, 3619–3622.

[46] A. Gładysiak, T. N. Nguyen, R. Bounds, A. Zacharia, G. Itskos, J. A. Reimer, K. C. Stylianou, *Chem. Sci.* **2019**, *10*, 6140–6148.

[47] K. Xue, C. Wang, J. Wang, S. Lv, B. Hao, C. Zhu, B. Z. Tang, *J. Am. Chem. Soc.* **2021**, *143*, 14147–14157.

[48] X. Yang, Y. Fu, M. Liu, S. Zheng, X. Li, Q. Xu, G. Zeng, *Angew. Chem. Int. Ed.* **2024**, *63*, e202319247.

[49] J. Cuan, H. Zhou, X. Huang, X. Cong, Y. Zhou, *Small* **2023**, *19*, e2305624.

[50] H. Zhao, J. Ni, J. J. Zhang, S. Q. Liu, Y. J. Sun, H. Zhou, Y. Q. Li, C. Y. Duan, *Chem. Sci.* **2018**, *9*, 2918–2926.

[51] M. J. Dong, M. Zhao, S. Ou, C. Zou, C. D. Wu, *Angew. Chem. Int. Ed.* **2014**, *53*, 1575–1579.

[52] Y. Zhang, X. Wang, K. Xu, F. Zhai, J. Shu, Y. Tao, J. Wang, L. Jiang, L. Yang, Y. Wang, W. Liu, J. Su, Z. Chai, S. Wang, *J. Am. Chem. Soc.* **2023**, *145*, 13161–13168.

[53] Z. W. Jiang, T. T. Zhao, S. J. Zhen, C. M. Li, Y. F. Li, C. Z. Huang, *J. Mater. Chem. A* **2021**, *9*, 9301–9306.

[54] M. Orfano, J. Perego, C. X. Bezuidenhout, I. Villa, R. Lorenzi, B. Sabot, S. Pierre, S. Bracco, S. Piva, A. Comotti, A. Monguzzi, *Adv. Funct. Mater.* **2024**, *34*, 2404480.

[55] J. W. Xue, C. H. Xu, W. Zhao, H. Y. Chen, J. J. Xu, *Nano Lett.* **2023**, *23*, 4572–4578.

[56] Y. Zhao, J. Descamps, N. al Hoda Al Bast, M. Duque, J. Esteve, B. Sepulveda, G. Loget, N. Sojic, *J. Am. Chem. Soc.* **2023**, *145*, 17420–17426.
[57] X. Hu, S. Yu, C. Wang, X. Zhang, J. Pan, H. Ju, *Anal. Chem.* **2023**, *95*, 4496–4502.
[58] M. M. Chen, C. H. Xu, W. Zhao, H. Y. Chen, J. J. Xu, *J. Am. Chem. Soc.* **2021**, *143*, 18511–18518.
[59] P. Zhao, W. Zhu, M. Zheng, J. Feng, *Anal. Chem.* **2023**, *95*, 4803–4809.
[60] J. Dong, Y. Xu, Z. Zhang, J. Feng, *Angew. Chem. Int. Ed.* **2022**, *61*, e202200187.
[61] J. Descamps, C. Colin, G. Tessier, S. Arbault, N. Sojic, *Angew. Chem. Int. Ed.* **2023**, *62*, e202218574.
[62] H. Liu, A. Hussain, Y. T. Zholudov, D. V. Snizhko, N. Sojic, G. Xu, *Angew. Chem. Int. Ed.* **2024**, *63*, e202411764.
[63] J. Han, X. He, J. Liu, R. Ming, M. Lin, H. Li, X. Zhou, H. Deng, *Chem* **2022**, *8*, 1637–1657.
[64] M. Zhao, J. Chen, B. Chen, X. Zhang, Z. Shi, Z. Liu, Q. Ma, Y. Peng, C. Tan, X. J. Wu, H. Zhang, *J. Am. Chem. Soc.* **2020**, *142*, 8953–8961.

Manuscript received: January 15, 2025
Revised manuscript received: February 26, 2025
Accepted manuscript online: March 03, 2025
Version of record online: ■■, ■■

Research Article

Electrochemiluminescence

Y. Wang, T. Liu, S. Yu, R. Luo, S. Bao,
J. Wu*, H. Ju, Z. Dai*, J. Lei* - **e202501151**

Polychromatic Electrochemiluminescence Imaging of Single Heteroligand Metal–Organic Crystals

We design a series of heteroligand MOFs composting of porphyrin and pyrene ligands as crystalline emitters for polychromatic ECL imaging. Due to rational conjugated spacing of MOF, it exhibits excellent energy transfer efficiency and unique polychromatic ECL imaging characteristics, providing the first instance of single MOF crystals in ECL imaging.